RSC Advances

ROYAL SOCIETY OF CHEMISTRY

www.rsc.org/advances

Facile synthesis of g-C_3N_4 isotype composite with enhanced visible-light photocatalytic activity

Lei Shi [2], Lin Liang [3], Fangxiao Wang [2], Mengshuai Liu [2], Jianmin Sun [1, 2] *

1. State Key Laboratory of Urban Water Resource and Environment, Harbin Institute of Technology, Harbin 150080, China

2. The Academy of Fundamental and Interdisciplinary Science, Harbin Institute of Technology, Harbin 150080, China

3. School of Life Science and Technology, Harbin Institute of Technology, Harbin 150080, China

*Corresponding author: Jianmin Sun

E-mail: sunjm@hit.edu.cn

Tel.:+86 451 86403715.

Abstract

A highly active g-C_3N_4 isotype composite was prepared with precursor mixture of melamine and thiourea by one-step thermal treatment. The differences in electronic band structure of as-prepared isotype g-C_3N_4 made the band levels match with each other. This novel metal-free isotype composite was demonstrated to promote the separation of photoinduced charges, leading to a significant enhancement in the photocatalytic activity for degrading Rhodamine B under visible-light irradiation. Moreover, the resultant g-C_3N_4 isotype composite possessed excellent stability after three recycles. Finally, the relevant mechanism for the photodegradation process was also proposed.

Keywords: g-C_3N_4; isotype composite; photocatalyst; visible light

1. Introduction

Visible-light semiconductor photocatalysts have attracted intensive interests due to their outstanding performance in conversion of solar energy, including clean energy production, [1] environmental remediation [2] and chemical synthesis. [3] In recent years, as a kind of visible-light responsive photocatalyst, graphitic carbon nitride (g-C_3N_4) has drawn great attention owing to its suitable band gap to absorb the visible light and unique properties in excellent performance in H_2 evolution via water splitting and degradation of organic pollutants under visible-light irradiation. [4-13] But unsatisfactorily, the photocatalytic efficiency was still restricted due to the high recombination rate of photogenerated electron-hole pairs. To overcome this trouble, many methods have been developed to improve the photocatalytic activity including nonmetal doping, [14] metal modifying, [15] coupling with semiconductor composite [16] and introducing mesopores. [17]

Recently, it was found that constructing isotype heterojunction between two different crystal phases of a single semiconductor was a simple and efficient strategy to promote the separation of photogenerated electrons and holes, such as α-β-phase Bi_2O_3 heterojunction [18] and anatase-rutile phase TiO_2 heterojunction. [19] Previous reports indicated that g-C_3N_4 was easily prepared by heating various structured precursors including urea, thiourea, melamine and cyanamide, et al. And the band gap of as-made g-C_3N_4 was facilely adjusted by selecting different precursors, which became the basis for constructing g-C_3N_4 isotype heterojunction. Wang et al prepared g-C_3N_4 isotype heterojunction with enhanced visible-light activity by coating the

precursor onto the surface of g-C_3N_4 then followed by further thermal treatment. [20] Dong et al. constructed g-C_3N_4/g-C_3N_4 isotype heterojunction with significant enhancements in the photocatalytic NO removal using urea and thiourea, or dicyandiamide (melamine) and urea as raw materials. [21, 22] Moreover, g-C_3N_4/S-g-C_3N_4 metal-free isotype heterojunction catalysts were also exploited. [23, 24] However, except for the few works reported by Dong et al, some synthesis strategies needed two-step thermal treatment processes, which were time-consuming and energy dissipation. In our continuous development of metal-free active photocatalysts for the treatment of wastewater, in the present contribution, g-C_3N_4 isotype composite was facilely prepared by directly heating the molecular mixtures of melamine and thiourea precursors for treatment of dye-containing wastewater. The isotype composite of C_3N_4-MT was fully confirmed by XRD, XPS, SEM, EDS, TEM and band gap differences, providing the solid evidences that the isotype composite of C_3N_4-MT was formed from the molecular composition precursors. The resultant g-C_3N_4 isotype composite exhibited better visible-light photocatalytic activity for degrading Rhodamine B (RhB) in water than separate single phase g-C_3N_4 and reference composite synthesized by two-steps. The enhanced photocatalytic performance could be ascribed to the efficient charge separation and transfer across the isotype composite interface. Moreover, the resultant g-C_3N_4 isotype composite possessed excellent stability after three recycles. The present synthesis method is economic, facile and environmentally benign, which opened the feasible and large-scaled fabrication avenue for the isotype composite in wide application fields especially in clean energy

production and pollutant remediation.

2. Experimental

2.1 Synthesis of photocatalysts

In a typical synthesis, 5 g of melamine and 5 g of thiourea were added into 30 mL distilled water. After stirring for 3 h, the mixture was dried at 60 °C to obtain the white composite precursor, which was transferred into crucible with a cover and heated to 550 ℃ at a heating rate of 3 ℃ min^{-1} for 2 h. For comparison, 10 g of melamine or 10 g of thiourea was treated separately under the same thermal conditions. The as-made g-C_3N_4 samples were respectively denoted as C_3N_4-M, C_3N_4-T and C_3N_4-MT according to the precursors of melamine, thiourea, and melamine-thiourea mixture used in the synthesis process.

Moreover, g-C_3N_4 isotype heterojunction was also prepared by two-steps method for comparison. [24] 2 g as-prepared C_3N_4-M and 5 g of thiourea were added into 30 mL distilled water and ultrasonically treated for 1 h, then stirred for 3 h. After the mixture heated at 60 °C to remove the water, the solid product was transferred into crucible with a cover and heated at 550 ℃ for 2 h. The obtained sample was denoted C_3N_4-MT(TS).

2.2 Material characterizations

The patterns of X-ray diffraction were carried out on a Bruker D8 Advance X-ray powder diffractometer with Cu Kα radiation (40 kV, 40 mA) for phase identification. Fourier transform infrared spectroscopy (FTIR) was recorded on a Perkin Elmer

spectrum 100 FTIR spectrometer using KBr discs. Morphologies were examined with scanning electron microscope (SEM, SU8010, Hitachi). The spatial elemental distributions were investigated by energy-dispersive spectrometry (EDS) elemental mapping analysis. The structure of the sample was examined by transmission electron microscopy (TEM, JEM-2010). X-ray photoelectron spectroscopy (XPS) measurements were recorded on a Thermo Fisher Scientific Escalab 250. The Brunauer-Emmett-Teller (BET) surface areas were collected at 77 K using a Micromeritics Tristar 3020 analyzer, samples were outgassed at 120 °C for 12 h prior to measurement. The UV-vis diffuse reflectance spectra (DRS) were measured on a Perkin Elmer Lambda 750 UV-vis spectrometer. The photoluminescence spectra (PL) were obtained by a Perkin Elmer LS55 spectrometer with an excitation wavelength of 325 nm.

2.3 Photocatalytic testing

The photocatalytic performance of the as-made samples was evaluated through degrading RhB dye under visible light. A 300 W Xe lamp with a 400 nm cutoff filter was used as the light source to provide visible-light irradiation. 100 mg resultant photocatalyst was dispersed into 100 mL 5 $mg \cdot L^{-1}$ RhB solution for photocatalytic examination under magnetic stirring. Prior to the light irradiation, the dispersion was kept in dark for 60 min under magnetic stirring to reach the adsorption-desorption equilibrium. Solutions after irradiation were collected every given time interval and centrifuged to remove the catalyst then analyzed on UV-vis spectrometer. The efficiency degradation was calculated by C/C_0, wherein C is the concentration of

remaining dye solution at each irradiated time, and C_0 is the initial concentration.

3. Results and discussion

Fig. 1 showed the X-ray diffraction patterns of the as-prepared C_3N_4-M, C_3N_4-T and C_3N_4-MT. The XRD patterns all proved the successful formations of g-C_3N_4 layers, two peaks were observed in the resultant g-C_3N_4 from the precursors of melamine, thiourea, and thiourea-melamine mixture. The peak at 13.0° ascribed to (100) plane were corresponded to in-plane structural packing motif. [12] The other peak around 27.4° was indexed to (002) plane of hexagonal g-C_3N_4 (JCPDS card no. 87-1526), indicating the graphite-like stacking of the conjugated aromatic units of CN. [10] From the magnifications of (002) peaks, C_3N_4-M and C_3N_4-T were slight different, separately corresponding to 27.38° and 27.52°. And the diffraction angle (002) peak of C_3N_4-MT was located at 27.43° between C_3N_4-M and C_3N_4-T, proving that C_3N_4-MT was composed of C_3N_4-M and C_3N_4-T.

(Fig. 1)

Fig. 2 displayed the similar FTIR spectra in the three samples of C_3N_4. The absorption peak at 810 cm^{-1} was considered as the out-of-plane skeletal bending modes of the triazine cycles, [17] and the absorption bands in the range of 1200-1700 cm^{-1} were assigned to the typical stretching modes of CN heterocycles. [16] The broad band centered at 3176 cm^{-1} was attributed to NH_2 or NH groups, which were originated from the incomplete condensation and the residual hydrogen atoms bonded to the edges of the graphene-like C–N sheet in the forms of C-NH_2 and 2C-NH

bonds.[25]

(Fig. 2)

Subsequently, the XPS spectra of C_3N_4-M, C_3N_4-T and C_3N_4-MT were investigated to detect the structure of g-C_3N_4. In the C 1s region (Fig. 3A), the peaks located at 288.2 eV for three samples were attributed to the presence of sp^2 C bonded N (C=N) in the aromatic rings. [26, 27] The main N 1s peak was deconvoluted into three peaks with binding energies of 398.9, 400.1 and 401.2 eV, assigned to sp^2 hybridized nitrogen (C=N–C), tertiary nitrogen (N–$(C)_3$) groups and amino functional groups (–NH_2 or –NH), respectively. [28-30] For S 2p XPS spectra, there was no S species in the C_3N_4-M, while S were located at 163.6 eV for C_3N_4-T and C_3N_4-MT, which meant that S was doped in g-C_3N_4-MT through the formation of S–C bond. [31] Besides, there was another weak peak at 169.8 eV in C_3N_4-T sample, possibly attributed to sulfur oxide species. [32] The band XPS structures of C_3N_4-M and C_3N_4-T was provided in Fig. 3D, the VB XPS maxima of C_3N_4-M and C_3N_4-T were revealed to be 1.60 and 1.48 eV, respectively.

(Fig. 3)

The morphologies of as-prepared C_3N_4-M, C_3N_4-T and C_3N_4-MT were investigated by SEM in Fig 4. It was observed that the morphologies of C_3N_4-M and C_3N_4-T were distinctively different. C_3N_4-M was composed of dense and thick layers to form the flat bulk, while C_3N_4-T consisted of curly and thinner sheets to generate the interconnected pores between stacked layers. The morphologic differences were explained that the different molecular structures of melamine and thiourea led to

different condensation forms during the polycondensation process. In the case of C_3N_4-MT, besides the dense bulk, the curly thinner layers were also clearly observed, indicating the composite was coupled with C_3N_4-T and C_3N_4-M. EDS analyses for C_3N_4-MT further confirmed the hybridization of C_3N_4-T and C_3N_4-M. For the curly and thinner layer area, the existence of C, N and S elements suggested the presence of C_3N_4-T, which were provided by the thermal polycondensation of thiourea source. [32] However, the elemental mapping for the dense and bulk area only revealed the existence of C and N, but the absence of S, which was regarded as C_3N_4-M base. The inhomogeneous distributions of S elements provided the solid evidence that C_3N_4-MT isotype composite was constituted by C_3N_4-M and C_3N_4-T.

Moreover, to further prove above result, the TEM images of C_3N_4-M, C_3N_4-T and C_3N_4-MT were investigated. A typical layered platelet-like surface morphology (Fig. 4F) and a curly nanostructure (Fig. 4G) were identified for C_3N_4-M and C_3N_4-T, respectively, consistent with the separate C_3N_4-M and C_3N_4-T morphologies. [33-35] Curly C_3N_4-T was packed and grafted closely onto the flat surface of C_3N_4-M, both them were integrated together to form the C_3N_4-MT composite (Fig. 4H). The existed different structures in the C_3N_4-MT composite would facilitate charge transfer between C_3N_4-M and C_3N_4-T, therefore, the improved separation rates for photogenerated charges and thus enhanced photocatalytic activity were anticipated. Moreover, BET surface areas of C_3N_4-M, C_3N_4-T and C_3N_4-MT were 6.5, 10.7 and 9.2 $m^2 g^{-1}$, respectively. C_3N_4-T and C_3N_4-MT presented the enhanced surface areas compared with C_3N_4-M, which would contribute to promoting the photocatalytic

activity.

(Fig. 4)

The UV-visible diffuse reflectance spectra of the samples were investigated in Fig. 5. It was observed that g-C_3N_4 prepared from melamine, thiourea, the mixture of melamine and thiourea have different absorption edges, estimated to 460, 492 and 475 nm, corresponding to the band gaps at 2.70, 2.52 and 2.61 eV, respectively. The optical absorption edge and band edge of C_3N_4-MT were located between those of C_3N_4-M and C_3N_4-T, further confirmed the electronic coupling of the two components in C_3N_4-MT composite. And compared with g-C_3N_4-M, g-C_3N_4-T and g-C_3N_4-MT possessed strong absorptions in visible light range and narrowed band gaps, which were resulted from S doping. [32] Hence, the remarkable differences in band gap energies of C_3N_4-M and C_3N_4-T provided feasible basis for the rational design of g-C_3N_4 isotype composite with well-matched band structure.

(Fig. 5)

The photocatalytic activities of as-prepared samples were evaluated by the photodegradation of RhB dye under visible-light irradiation. As Fig 6 depicted, the degradation RhB hardly carried out even for 1 h without any catalyst, while only 36%, 60% and 49% RhB were degraded over C_3N_4-M, C_3N_4-T and C_3N_4-MT(TS) samples under the same conditions, respectively. Noticeably, the as-prepared C_3N_4-MT possessed much better photocatalytic activity, almost 90% RhB was degraded within 1 h.

(Fig. 6)

The stability is another vital consideration for the photocatalyst except for the

photocatalytic activity. Hence, the recycling degradation experiments over C_3N_4-MT were carried out in Fig 7. After each run, the catalyst was collected and washed with water and ethanol, then reused for the next run. The photocatalytic activity was still almost the same to the fresh catalyst even after three recycles, suggesting the excellent stability of the C_3N_4-MT photocatalyst.

(Fig. 7)

In addition, the structure of catalyst was further measured after the three photodegradation runs by XRD and FTIR. Fig. 8A diaplayed XRD patterns of C_3N_4-MT before and after the repeated photocatalytic reactions. The XRD pattern of the reused C_3N_4-MT was similar to the fresh catalyst, meaning that the C_3N_4-MT was stable during the photoreaction process. However, the spent C_3N_4-MT exhibited the lower and broader diffraction intensity, which was resulted from the narrowed interplanar distance and/or interlayer stacking distance of C_3N_4-MT after three recycles. [10] Similarly, as found from Fig. 8B, the FTIR of C_3N_4-MT after photodegradation was almost unaltered, further proving the stability of the photocatalyst.

(Fig. 8)

Compared with C_3N_4-M and C_3N_4-T photocatalysts, it was obvious that C_3N_4-MT exhibited the improved photocatalytic activity, which was attributed to effective interfacial effect between C_3N_4-M and C_3N_4-T, facilitating the photogenerated electron transfers from C_3N_4-M to C_3N_4-T, thus reducing the photogenerated electron-hole recombination rates greatly. In order to fully understand

the photocatalytic mechanism of C_3N_4-MT isotype composite, the valence band (VB) and conduction band (CB) potentials of C_3N_4-M and C_3N_4-T were estimated according to the following empirical equations. [36]

$$E_{VB} = X - E^e + 0.5\ Eg \quad (1)$$

$$E_{CB} = E_{VB} - Eg \quad (2)$$

where E_{VB} is the valence band edge potential, E_{CB} is the conduction band edge potential, X is the electronegativity of the semiconductor, which is the geometric mean of the electronegativity of the constituent atoms, and the X value for g-C_3N_4 is ca. 4.73 eV, [37] E^e is the energy of free electrons on the hydrogen scale at about 4.5 eV, [38] Eg is the band gap energy of the semiconductor. The band gaps of C_3N_4-M and C_3N_4-T were 2.70 and 2.52 eV, respectively. Hence, according to above empirical equations, the CB and VB edge potentials of C_3N_4-M were calculated at -1.12 and +1.58 eV, whereas, those of C_3N_4-T were at -1.03 and +1.49 eV, respectively. In addition, based on the VB XPS in Fig. 3D, the CB potentials of C_3N_4-M and C_3N_4-T were calculated at -1.10 and -1.04 eV. Thus, the band energy levels of C_3N_4-M at -1.10 and +1.60 eV and those of C_3N_4-T at -1.04 and +1.48 eV were consistent with the empirical equations calculations. Thus, on the basis of VB and CB levels of C_3N_4-M and C_3N_4-T, the schematic illustration of electron-hole separation and transport at the interface of C_3N_4-MT composite was shown in Fig 9A. When C_3N_4-MT was irradiated by visible light, photogenerated electrons (e^-) in the conduction band and the same amounts of holes (h^+) in the valence band were excited. The CB edge potentials of C_3N_4-M were more negative than those of C_3N_4-T, which

allowed the electrons to easily transfer from the C_3N_4-M to C_3N_4-T and separate electron-hole pairs efficiently. Then e^- combined with O_2 to form $\bullet O_2^-$, which reacted with H_2O to further form the active species •OH. [39] On the other hand, the VB potentials of C_3N_4-M and C_3N_4-T were less positive than the standard redox potential of $\bullet OH/H_2O$ (2.68 eV vs. SHE), [40] indicating that the photogenerated holes could not oxidize H_2O into •OH. Photogenerated holes would be directly involved into the degradation of RhB. Therefore, the generated h^+, e^-, $\bullet O_2^-$ and •OH reacted with the organic dye to generate the degradation products. Thus, in the photocatalysis process, the separation efficiency of electron-hole pairs was promoted due to the existed isotype hybridization in C_3N_4-MT composite, subsequently improved the photocatalytic efficiency.

The PL spectra of C_3N_4-M, C_3N_4-T and C_3N_4-MT with the excitation wavelength of 325 nm were investigated in Fig 9B. The pristine C_3N_4-M had a strong PL emission peak, while C_3N_4-T exhibited the lowest PL emission peak, possibly more structural imperfections in C_3N_4-T led to a reduced radiative PL emission. [35, 41] But by coupling with C_3N_4-T, C_3N_4-MT composite displayed low charge recombination. Hence, the intrinsic drawbacks of fast charge recombination in g-C_3N_4 could be solved through the construction of isotype composite.

(Fig. 9)

4. Conclusion

In conclusion, C_3N_4-MT isotype composite was prepared facilely with the

precursor mixture of melamine and thiourea by one-step thermal treatment. The differences in electronic band structures between C_3N_4-M and C_3N_4-T make this novel metal-free isotype C_3N_4-MT composite improve charge separation, thus resulting in a significant enhancement in the photocatalytic activity for degrading RhB under visible-light irradiation. The present facile and one-step synthesis method for isotype C_3N_4-MT composite supplied new perspective that other isotype semiconductors can be easily and large-scaled fabrication for sustainable utilizations of solar energy.

Acknowledgement

We sincerely acknowledge the financial supports from National Natural Science Foundation of China (21373069), Science Foundation of Harbin City (NJ20140037), State Key Lab of Urban Water Resource and Environment of Harbin Institute of Technology (HIT2015DX08) and the Fundamental Research Funds for the Central Universities (HIT. IBRSEM. 201327).

References

1. X. Chen, L. Liu, P. Y. Yu and S. S. Mao, *Science*, 2011, **331**, 746-750.
2. Y. Wang, X. Wang and M. Antonietti, *Angew. Chem. Int. Ed.,* 2012, **51**, 68-89.
3. X. Wang, S. Blechert and M. Antonietti, *ACS Catal.*, 2012, **2**, 1596-1606.
4. X. C. Wang, K. Maeda, A. Thomas, K. Takanabe, G. Xin, J. M. Carlsson, K. Domenet and M. Antonietti, *Nat. Mater.,* 2009, **8**, 76-80.
5. H. Yan, *Chem. Commun.,* 2012, **48**, 3430-3432.

6. X. C. Wang, K. Maeda, X. Chen, K. Takanabe, K. Domen, Y. Hou, X. Fu and M. Antonietti, *J. Am. Chem. Soc.*, 2009, **131**, 1680-1681.

7. S. C. Lee, H. O. Lintang and L. Yuliati, *Chem. Asian J.,* 2012, **7**, 2139-2144.

8. Z. Zhao, Y. Sun and F. Dong, *Nanoscale,* 2015, **7**, 15-37.

9. S. Kumar, T. Surendar, A. Baruah and V. Shanker, *J. Mater. Chem. A,* 2013, **1**, 5333-5340.

10. L. Shi, L, Liang, J. Ma, F. X. Wang and J. M. Sun, *Dalton Trans.,* 2014, **43**, 7236-7244.

11. M. Tahir, C. Cao, F. K. Butt, F. Idrees, N. Mahmood, Z. Ali, I. Aslam, M. Tanveer, M. Rizwan and T. Mahmood, *J. Mater. Chem. A,* 2013, **1**, 13949-13955.

12. L. Shi, L. Liang, J. Ma, F. X. Wang and J. M. Sun, *Catal. Sci. Technol.,* 2014, **4**, 3235-3243.

13. W. Peng and X. Li, *Catal. Commun.,* 2014, **49**, 63-67.

14. G. Zhang, M. Zhang, X. Ye, X. Qiu, S. Lin and X. Wang, *Adv. Mater.,* 2014, **26**, 805-809.

15. L. Ge, C. Han, X. Xiao and L. Guo, *Appl. Catal. B: Environ.,* 2013, **142-143**, 414-422.

16. L. Shi, L. Liang, F. X. Wang, M. S. Liu and J. M. Sun, *J. Mater. Sci.,* 2015, **50**, 1718-1727.

17. L. Shi, L. Liang, F. X. Wang, M. S. Liu, S. F. Zhong and J. M. Sun, *Catal. Commun.*, 2015, **59**, 131-135.

18. J. Hou, C. Yang, Z. Wang, W. Zhou, S. Jiao and H. Zhu, *Appl. Catal. B: Environ.,* 2013, **142-143**, 504-511.

19. J. Zhang, Q. Xu, Z. C. Feng, M. J. Li and C. Li, *Angew. Chem. Int. Ed.,* 2008, **47**, 1766-1769.

20. J. Zhang, M. Zhang, R. Q. Sun and X. C. Wang, *Angew. Chem. Int. Ed.,* 2012, **51**, 1014-10149.

21. F. Dong, Z. Zhao, T. Xiong, Z. Ni, W. Zhang, Y. Sun and W. K. Ho, *ACS Appl. Mater. Interfaces*, 2013, **5**, 11392-11401.

22. F. Dong, Z. Ni, P. Li and Z. Wu, *New J. Chem.,* 2015, *39*, 4737-4744.

23. H. B. Tao, H. B. Yang, J. Chen, J. Miao and B. Liu, *Beilstein J. Nanotechnol.,* 2014, **5**,770-777.

24. S. Hu, L. Ma, F. Li, Z. Fan, Q. Wang, J. Bai, X. Kang and G. Wu, *RSC Adv.,* 2015, **5**, 90750-90756.

25. Y. C. Zhao, Z. Liu, W. G. Chu, L. Song, Z. X. Zhang, D. L. Yu, Y. J. Tian, S. S. Xie and L. F. Sun, *Adv. Mater.,* 2008, **20**, 1777-1781.

26. L. Shi, L. Liang, F. X. Wang, M. S. Liu, T. Liang, K. L. Chen and J. M. Sun, *RSC Adv.,* 2015, **5**, 63264-63270.

27. S. Cao, J. Low, J. Yu and M. Jaroniec, *Adv. Mater.,* 2015, **27**, 2150-2176.

28. Y. Qin, J. Li, J. Yuan, Y. Kong, Y. Tao, F. Lin and S. Li, *J. Power Sources,* 2014, **272**, 696-702.

29. L. Shi, T. Liang, L. Liang, F. X. Wang, M. S. Liu and J. M. Sun, *J. Porous Mater.,* 2015, **22**, 1393-1399.

30. Y. Yang, W. Guo, Y. N. Guo, Y. Zhao, X. Yuan and Y. H. Guo, *J. Hazard. Mater.,* 2014, **271**, 150-159.

31. G. Liu, P. Niu, C. Sun, S. C. Smith, Z. Chen, G. Q. Lu and H. M. Cheng, *J. Am. Chem. Soc.,* 2010, **132**, 11642-11648.

32. J. Hong, X. Xia, Y. Wang and R. Xu, *J. Mater. Chem.,* 2012, **22**, 15006-15012.

33. S. W. Cao, Y. P. Yuan, J. Fang, M. M. Shahjamali, F. Y. C. Boey, J. Barber, S. C. J. Loo and C. Xue, *Int. J. Hydrogen. Energy.,* 2013, **38**, 1258-1266.

34. S. Zhao, S. Chen, H. Yu and X. Quan, *Sep. Purif. Technol.,* 2012, **99**, 50-54.

35. F. Dong, Y. Sun, L. Wu, M. Fu and Z. Wu, *Catal. Sci. Technol.,* 2012, **2**, 1332-1335.

36. C. Xing, Z. Wu, D. Jiang and M. Chen, *J. Colloid Interface. Sci.,* 2014, **433**, 9-15.

37. W. Zhang, Y. Sun, F. Dong, W. Zhang, S. Duan and Q. Zhang, *Dalton Trans.,* 2014, **43**, 12026-12036.

38. D. Jiang, J. Zhu, M. Chen and J. Xie, *J. Colloid Interface Sci.,* 2014, **417**, 115-120.

39. F. Dong, Z. Wang, Y. Li, W. K. Ho and S. C. Lee, *Environ. Sci. Technol.,* 2014, **48**, 10345-10353

40. L. Shi, L. Liang, J. Ma, F. X. Wang and J. M. Sun, *Catal. Sci. Technol.,* 2014, **4**, 758-765

41. F. Dong, Z. Wang, Y. Sun, W. K. Ho and H. Zhang, *J. Colloid Interface. Sci.,* 2013, **401**, 70-79.

Figure Captions

Fig. 1. X-ray diffraction patterns (Inset is enlarged view of the (002) peak).

Fig. 2. FTIR spectra of (a) C_3N_4-M, (b) C_3N_4-T and (c) C_3N_4-MT.

Fig. 3. XPS spectra of (A) C 1s, (B) N 1s, (C) S 2p and (D) VB XPS spectra for (a) C_3N_4-M, (b) C_3N_4-T and (c) C_3N_4-MT.

Fig. 4. SEM images of (A) C_3N_4-M, (B) C_3N_4-T and (C) C_3N_4-MT; (D)-(E) EDS mappings for the rectangle areas; TEM images of (F) C_3N_4-M, (G) C_3N_4-T and (H) C_3N_4-MT.

Fig. 5. UV-visible diffuse reflectance spectra of (a) C_3N_4-M, (b) C_3N_4-T and (c) C_3N_4-MT.

Fig. 6 The photodegradation curves of RhB over as-prepared samples, (a) C_3N_4-M, (b) C_3N_4-T, (c) C_3N_4-MT, (d) C_3N_4-MT(TS) and (e) Without catalyst.

Fig. 7. Recycling runs in the photodegradation of RhB over C_3N_4-MT.

Fig. 8. (A) XRD patterns (Inset is enlarged view of the (002) peak) and (B) FTIR spectra of C_3N_4-MT before and after the photocatalytic reactions.

Fig. 9. (A) Schematic illustration of electron-hole separation and transport at the interface of C_3N_4-MT and the proposed photodegradation process of RhB; (B) Photoluminescence spectra of (a) C_3N_4-M, (b) C_3N_4-T and (c) C_3N_4-MT.

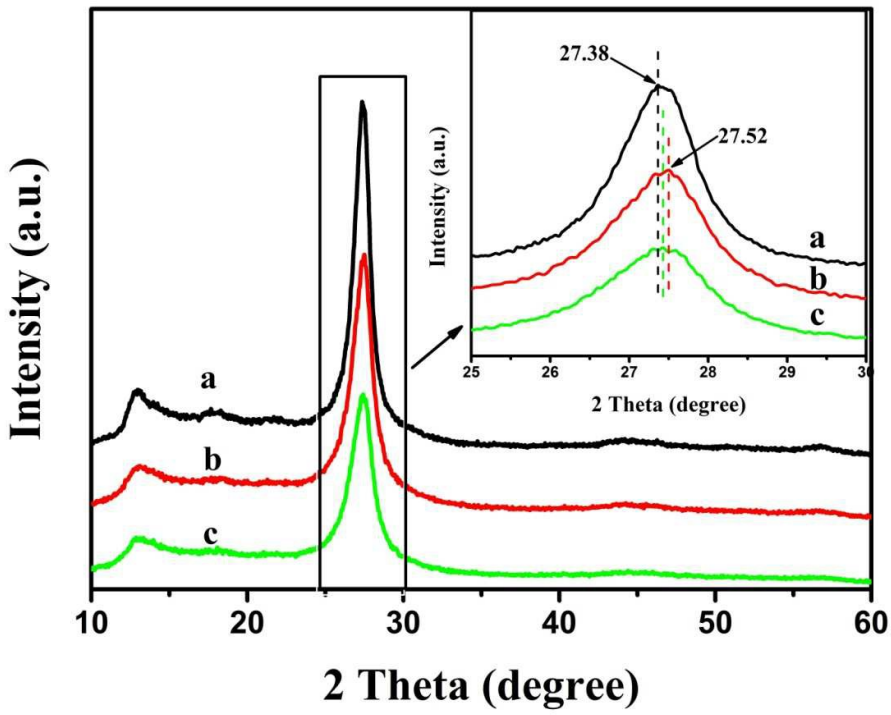

Fig. 1

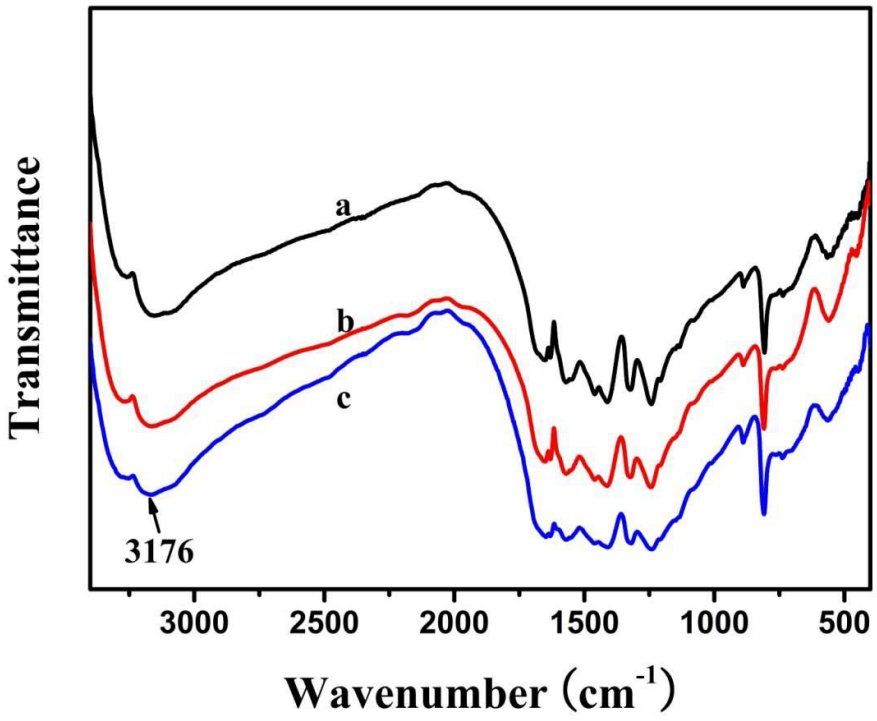

Fig. 2

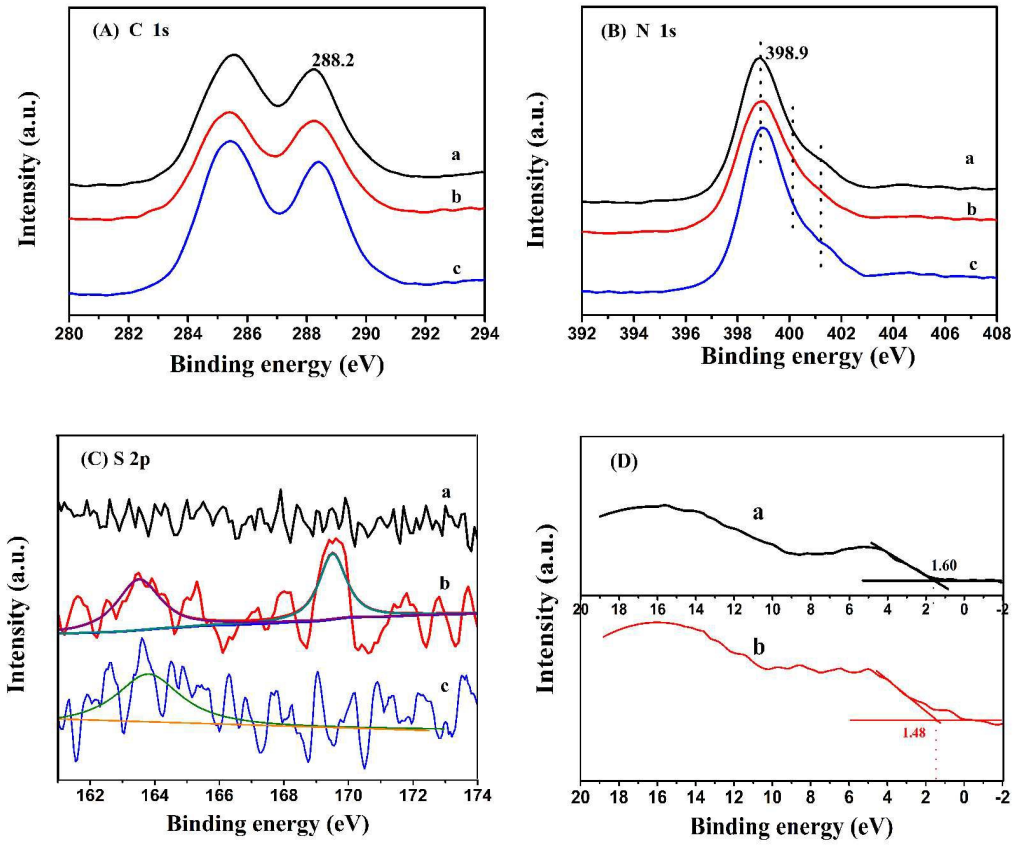

Fig. 3

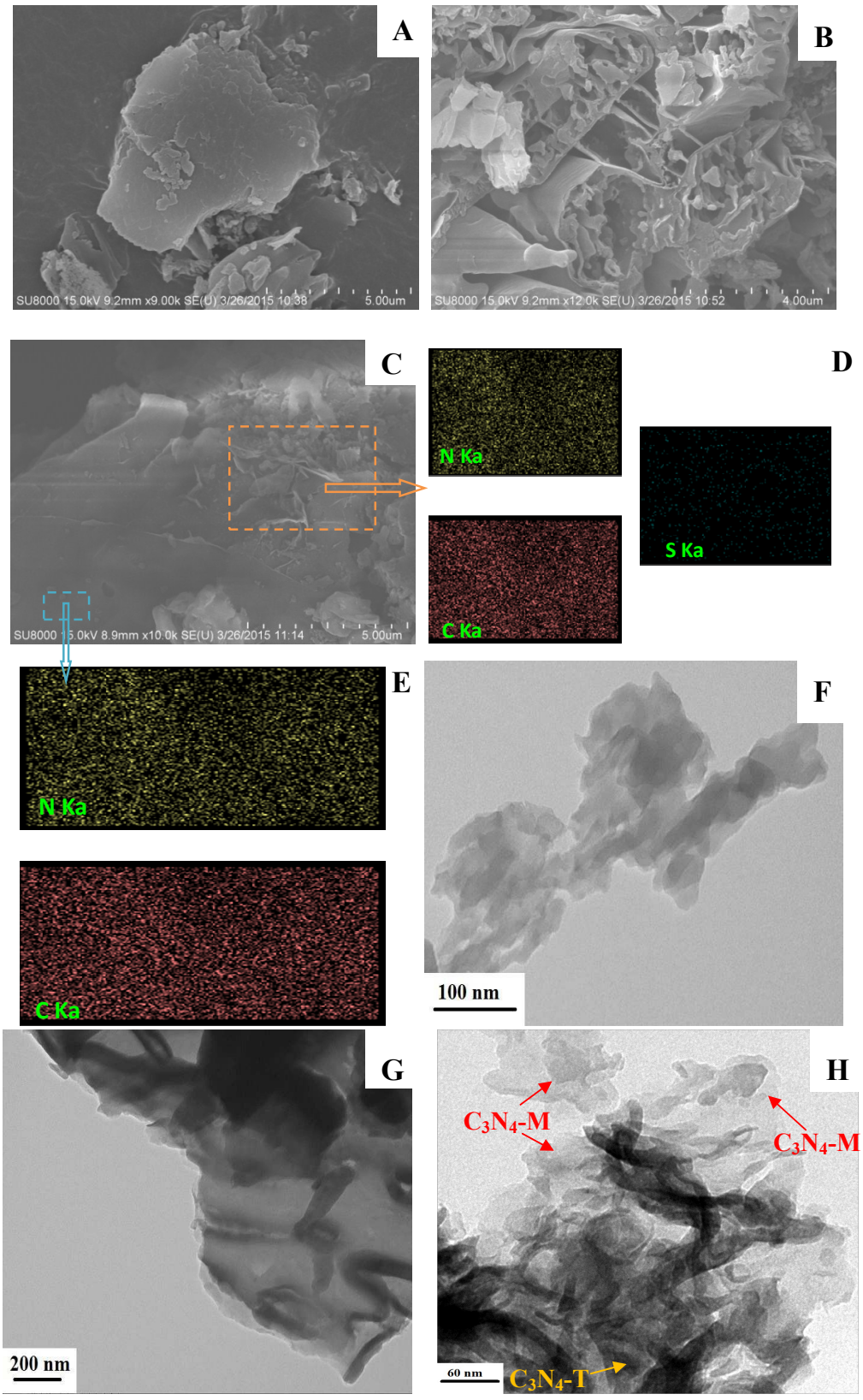

Fig. 4

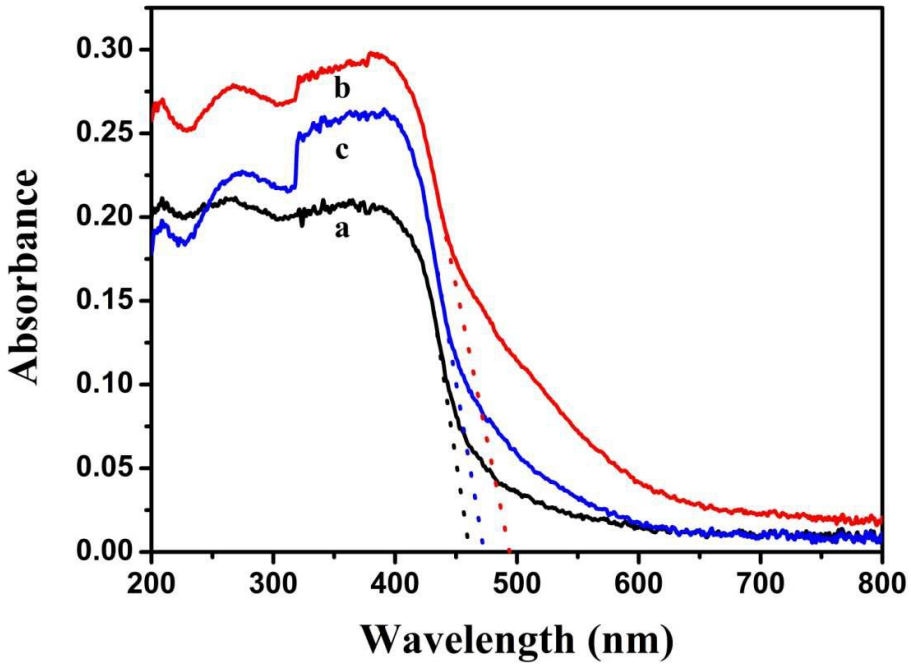

Fig. 5

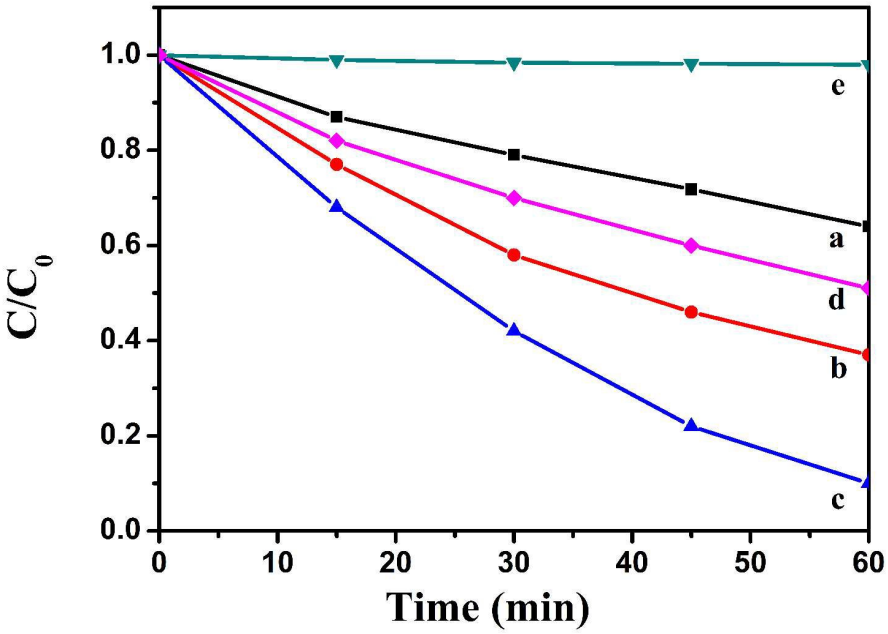

Fig. 6

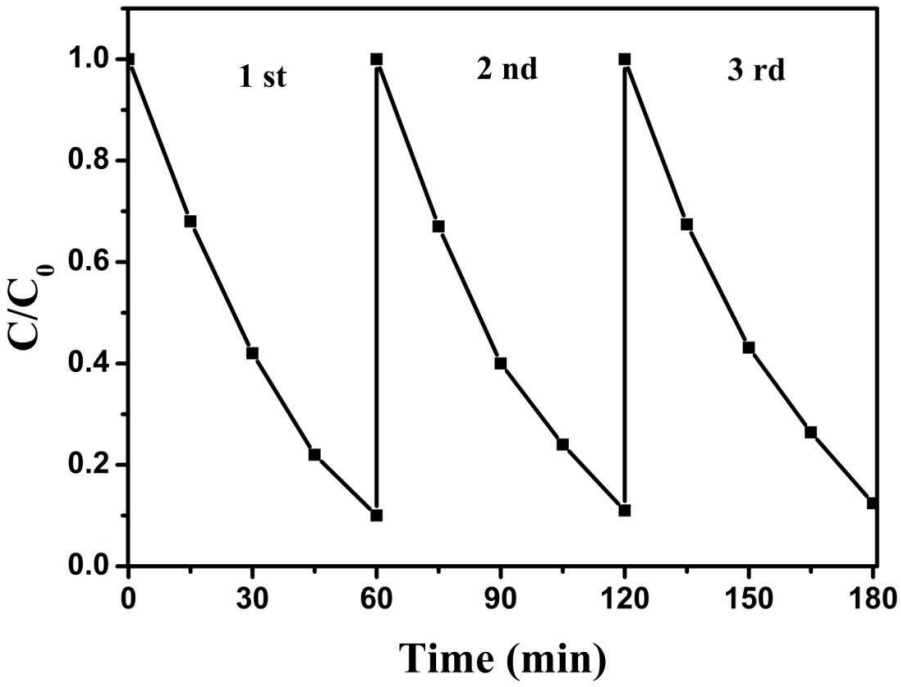

Fig. 7

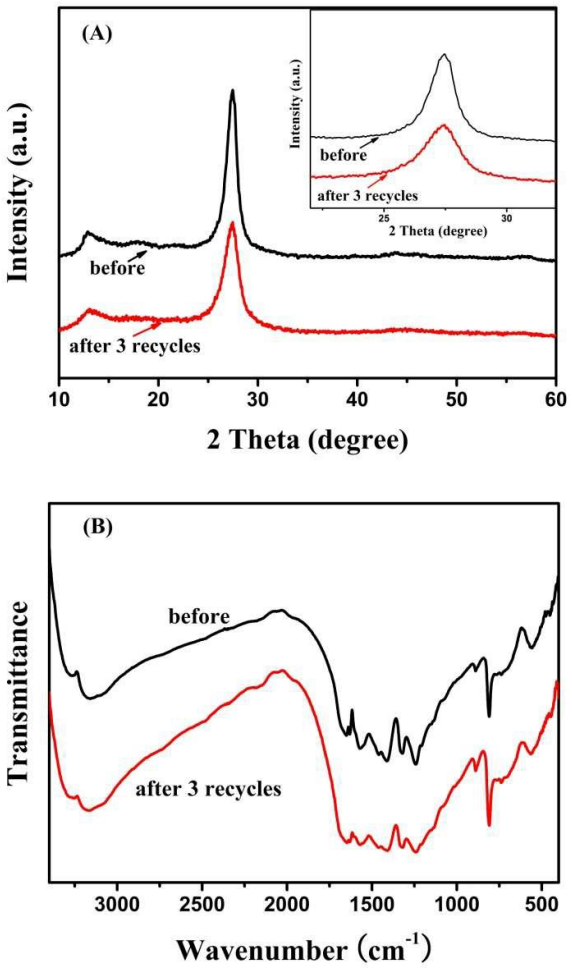

Fig. 8

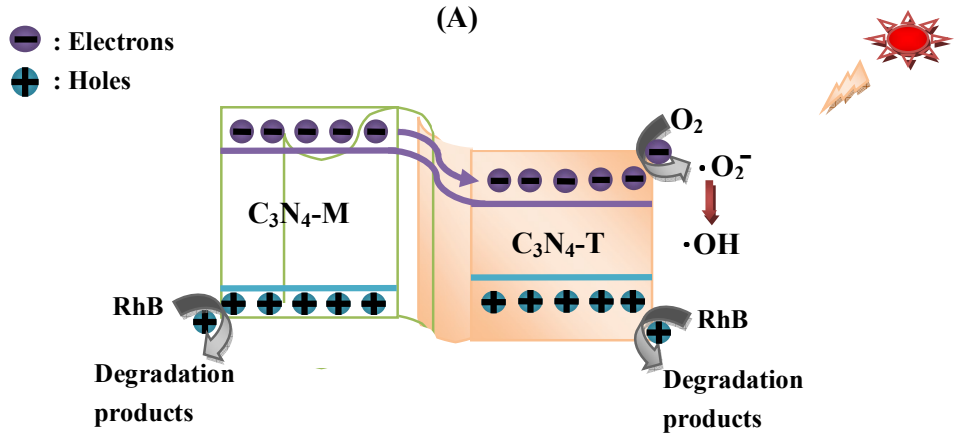

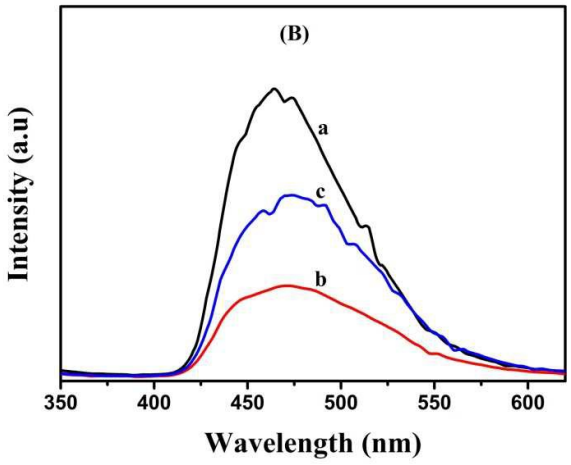

Fig. 9

Graphic abstract

The novel metal-free g-C_3N_4 isotype composite was successfully prepared and presented significant enhancement in the photocatalytic activity